Plant Physiology®

Plant Physiology, 2025, **199**, kiaf392
https://doi.org/10.1093/plphys/kiaf392
Advance access publication 1 September 2025
Research Article

The N-terminal domain of COMPANION OF CELLULOSE SYNTHASE1 promotes microtubule array formation in Arabidopsis

Viswanathan Gurumoorthy,[1] Alan Hicks,[2] Sriram Tiruvadi-Krishnan,[3] Wellington C. Leite,[4] Shirish Chodankar,[5] Jaydeep L. Kolape,[6] Jeremy C. Smith,[2,3] Rajan Lamichhane,[3] Hugh O'Neill[4,*]

[1]UT/ORNL Graduate School of Genome and Science Technology, University of Tennessee, Knoxville, TN 37996, USA
[2]UT/ORNL Center for Molecular Biophysics, Oak Ridge National Laboratory, Oak Ridge, TN 37831, USA
[3]Department of Biochemistry & Cellular and Molecular Biology, University of Tennessee, Knoxville, TN 37996, USA
[4]Neutron Scattering Division, Oak Ridge National Laboratory, Oak Ridge, TN 37831, USA
[5]LiX beamline, National Synchtron Light Source II, Brookhaven National Laboratory, Upton, NY 11973, USA
[6]Advanced Microscopy and Imaging Center, University of Tennessee, Knoxville, TN 37996, USA
*Author for correspondence: oneillhm@ornl.gov

The author responsible for distribution of materials integral to the findings presented in this article in accordance with the policy described in the Instructions for Authors (https://academic.oup.com/plphys/pages/General-Instructions) is Hugh O'Neill (oneillhm@ornl.gov).

Abstract

Microtubule-associated proteins (MAPs) play important roles in cellulose biosynthesis in plants. However, the molecular mechanisms mediating their interactions with cortical microtubule (MT) arrays remain to be elucidated. Here, we investigated the companion of cellulose synthase 1 (CC1), an Arabidopsis (*Arabidopsis thaliana*) MAP that stabilizes cellulose biosynthesis during salt stress by maintaining the integrity of the cortical MT array. The N-terminal domain of CC1 (CC1NTD) is sufficient to restore cellulose biosynthesis in Arabidopsis *cc1cc2* knockout mutants. We used a combination of small-angle X-ray and neutron scattering (SAXS and SANS), single-molecule Förster resonance energy transfer, and computational modeling to determine the structural characteristics of CC1NTD and its interactions with MTs. SANS measurements combined with deuterium labeling of CC1NTD allowed the structural features of CC1NTD and MTs to be deconvoluted and analyzed separately. CC1NTD bound to the MT surface and promoted interactions between neighboring MTs to form tightly associated arrays. In addition, CC1NTD appeared to be in an extended conformation during MT interactions, which could be important for forming cross-bridges between MTs during salt stress. Overall, this study provides structural insights into the mechanisms associated with a disordered MT-binding region in an MAP and provides an explanation for CC1's efficient organization of MTs, highlighting its importance in cellulose biosynthesis under stress conditions.

Introduction

Microtubules (MTs) are the primary component of the eukaryotic cytoskeleton and support and maintain the cell shape while also playing important roles in cellular functions such as cell division and cell motility, as well as guiding intracellular transport of proteins, ligands, and vesicles. MT structure is very well conserved across taxa and is composed of α- and β-tubulin heterodimers, which polymerize into hollow cylindrical tubes (Brouhard and Rice 2018; Goodson and Jonasson 2018). In addition, they are very dynamic complexes that undergo structural reorganization through depolymerization and repolymerization events in response to cellular processes that are controlled by microtubule-associated proteins (MAPs). MAPs are broadly classified as either motor proteins or nonmotor structural MAPs (Bodakuntla et al. 2019): motor proteins, such as dynein or kinesin transport molecules along MTs, while structural MAPs, such as tau and stathmin, are proteins that stabilize and/or destabilize the MT structure (Wen et al. 2010; Zhernov et al. 2020). Many structural MAPs have been identified as having roles in MT-related diseases. For instance, tau, a well-known human structural MAP, is involved in stabilizing MTs but when produced as a truncated mutant form in the brain, tau aggregates forming fibril structures that prevent its interaction with MTs and has been implicated in several neurodegenerative diseases, including Pick's disease and cerebral palsy, that are collectively known as tauopathies (Morris et al. 2011; Arendt et al. 2016). Similarly, in spinal muscular atrophy, a motor neuron disorder, upregulated levels of stathmin impair the formation of MT assemblies (Wen et al. 2010). Thus, it is important to understand MAP structure as well as the interactions that affect MT assembly and dynamics.

Plants also possess plant-specific MAPs that regulate plant cell morphology and physiology (Gardiner 2013). Plant MTs appear as bundled arrays close to the plasma membrane near the cell cortex and are therefore known as cortical MTs. During cell elongation, cortical MTs guide the orientation of newly synthesized cellulose microfibrils in the cell wall (Green 1980). However, the relationship between cortical MT arrangement and cellulose organization

Received April 15, 2025. Accepted July 14, 2025.
Published by Oxford University Press on behalf of American Society of Plant Biologists 2025.

is complex, and the roles of MAPs in mediating MT plasma membrane interactions are not fully understood (Dixit and Cyr 2004). Many MAPs are known to be intrinsically disordered proteins (IDPs) or possess extensive intrinsically disordered regions (IDRs) that play roles in facilitating interactions with MTs (Guharoy et al. 2013). The IDRs are proposed to enable structural flexibility and support multiple binding interactions that are important for fine-tuning MT dynamics. A recent review catalogued plant MAPs with IDRs in the context of their roles in MT interactions, including stabilization, organization, and response to environmental stimuli (Gonzalez et al. 2023). They reported that stretches of amino acids (7 to 12 residues) known as short linear motifs (SLiMs) may be directly or indirectly involved in facilitating weak but dynamic interactions with MTs (Gonzalez et al. 2023). For instance, QWRF is a well-conserved SLiM in plant MAPs such as endosperm defective 1 and augmin 8 that play an important role in plant growth and development (Pignocchi et al. 2009; Albrecht et al. 2010). Interestingly, bioinformatic analyses reveal that QWRF motifs are present in the IDR of these proteins (Gonzalez et al. 2023). Another example is the Arabidopsis (*Arabidopsis thaliana*) AtMAP65 protein family, which is important for maintaining cortical MT assemblies (Gaillard et al. 2008; Lucas et al. 2011). The dimeric form of AtMAP65-1 from this family promotes MT stabilization and bundling through binding of the C-terminal IDRs with the MTs (Li et al. 2007). Phosphorylation at the C-terminus has been shown to reduce the MT bundling function of this protein (Sasabe et al. 2006; Smertenko et al. 2006), highlighting the importance of posttranslational modifications in MAP functions.

Plant cells have a specialized set of MAPs that are involved in connecting cortical MTs to the cellulose synthesis complex (CSC) and helping in maintaining MT structure and organization. One example is the cellulose synthase interacting (CSI) family of proteins that have at least 3 isoforms (CSI-1, -2, and -3) in Arabidopsis. CSI-1 has been shown to interact with the cortical MTs and colocalize with cellulose synthase A (CESA) proteins in the plasma membrane (Gu et al. 2010). It has been proposed that this family of proteins links MTs to the CSC to facilitate its movement in the plasma membrane. However, even in *csi1-3* knockout mutants, CESA proteins were still able to traverse along MTs (Gu et al. 2010), suggesting that there could be other MAPs that play roles in connecting CESA proteins to MT arrays (Lei et al. 2014). Many studies have highlighted the lack of molecular details in understanding how MAPs are involved in cellulose synthesis and the role of cortical MT arrays and their association with the plasma membrane in this process (Yang et al. 2019; Ma et al. 2021). Furthermore, although the functional importance of MAPs has been demonstrated, the mechanisms by which they interact with cortical MT arrays or how MAPs help in stabilizing and assembling MTs are poorly understood (Hashimoto 2015; Elliott and Shaw 2018). Elucidating the structural details on how plant MAPs interact with MTs will shed light on other MT-associated processes, such as cellulose synthesis and plant growth.

In this study, we focus on the companion of cellulose synthase (CC) protein MAP family, which has been identified as playing a role in supporting cellulose synthesis during exposure to salt stress conditions in Arabidopsis. Knockout mutants of combinations of 4 members of this family (CC1 to 4) were generated that included single, double, triple, and tetra-knockout mutants—these showed that only the plants that had both CC1 and CC2 mutations showed a phenotype. These plants presented as shorter hypocotyls compared with the wild type. In addition, when *cc1cc2* plants were supplemented with 150 mM NaCl (mimicking salt stress) during growth, cellulose synthesis was greatly reduced, suggesting a role for CC1 and CC2 in maintaining cellulose synthesis during stress conditions. This is also supported by an in vivo split ubiquitin assay that showed CC1 interacts with CESA1, CESA3, and CESA6 (Endler et al. 2015). Finally, *cc1cc2* plants also displayed disorganized MT arrays under salt stress, supporting the fact that CC proteins are important in maintaining cortical MT arrays (Endler et al. 2015).

Of the CC proteins identified in Arabidopsis, only the properties of CC1 have been extensively characterized (Endler et al. 2015; Endler et al. 2016; Kesten et al. 2019a , 2019b). Based on the analysis of its amino acid sequence, CC1 has 3 major domains: an intrinsically disordered cytosolic domain (aa 1 to 120), a putative transmembrane domain (aa 130 to 152), and a C-terminal folded domain (aa 153 to 342) that is thought to be in the intercellular apoplast region, as shown in Fig. 1 (Endler et al. 2015). The CC1 cytoplasmic N-terminal region (CC1NTD) interacts with MTs both in vitro and in vivo (Endler et al. 2015; Kesten et al. 2019b). In *cc1cc2* knockout Arabidopsis mutants in which the CC1NTD has been reintroduced, plants were rescued from growth defects (Endler et al. 2015). Previously, CC1NTD was found to diffuse along MTs, and using NMR, 4 hydrophobic motifs (R23-S30, F45-M54, F74-G83, and Q103-I110) were identified as being important for interactions with MTs (Supplementary Fig. S1A; Kesten et al. 2019b). In particular, 2 tyrosine residues (Y26Y27) are required for MT interactions (Kesten et al.2019b). In addition, several phosphorylation sites have been identified in CC1NTD whose roles remain unknown (Colin et al. 2023). Confocal imaging and electron microscopy experiments also showed that the CC1NTD bundles MTs (Kesten et al. 2019b). Despite the functional importance of CC1, the lack of structural information about this protein has impeded the investigation of its mechanism of action and how it interacts with MTs to prevent their disintegration during salt stress.

The overall goal of the present study was to improve our understanding of the role of CC1 as a plant MAP. We investigated CC1NTD using a combination of small-angle X-ray and neutron scattering (SAXS and SANS) as well as fluorescence microscopy and electron microscopy to determine the structural characteristics of this CC1 domain and its interactions with MTs. SANS measurements that were combined with deuterium-labeling of the recombinantly expressed CC1NTD protein and computational modeling allowed the structural features of the CC1NTD and MTs to be deconvoluted and analyzed separately. The results show that CC1NTD binds to the surfaces of the MTs and promotes interactions between neighboring MTs to form tightly associated arrays. In addition, the CC1NTD appears to be in an extended conformation during MT interactions, which could be important for forming cross-bridges between MTs during salt stress. The unstructured nature of IDRs poses challenges for structural studies of MAPs, complicating efforts to determine their mechanism and role. This study shows how combining multiple structural techniques can provide structural insights into the mechanism of action of a disordered MT-binding region in an MAP and paves the way for future studies of flexible and disordered proteins that interact with MTs.

Results

Bioinformatics analysis of Arabidopsis CC1

Previous analyses of CC1 have shown that the N-terminal domain (CC1NTD, 1 to 120 aa) is an IDR and predicted that CC1 has a putative transmembrane domain and an apoplastic region

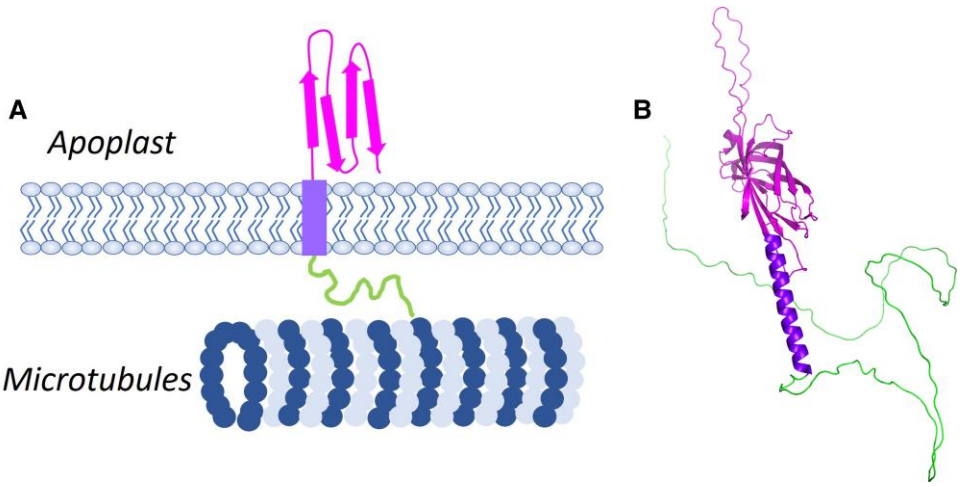

Figure 1. Structural model of Arabidopsis CC1. **A)** Schematic illustration of full-length CC1 with CC1NTD interacting with MTs. **B)** AlphaFold2 model of CC1 with the disordered region CC1NTD (1 to 120) in green, transmembrane region TM (121 to 150) in purple, and apoplastic region (151 to 343) in pink.

(Supplementary Fig. S1A) (Endler et al. 2015; Kesten et al. 2019b). The CC1 amino acid sequence was analyzed using different bioinformatic tools to learn more about its structural features. The Consensus Constrained TOPology (CCTOP) algorithm predicts putative transmembrane alpha helix regions in proteins from their amino acid sequence and also their topology for membrane insertion (Dobson et al. 2015). Using this approach, the full-length CC1 was found to have a single transmembrane helix region (residues 130 to 152) with the N-terminal end of the protein in the cytosol and the C-terminal end in the extracellular space or apoplast (Supplementary Fig. S1B). An ab initio structural model of full-length CC1 was obtained using Alphafold2 (Jumper et al. 2021; Varadi et al. 2022) and showed that the apoplastic region is rich in beta sheets and that there is a single alpha-helix in the same position predicted by CCTOP (Supplementary Fig. S1C). These domains of CC1 are predicted with high confidence based on the predicted local distance difference test score (pLDDT > 90%) computed for every residue (Mariani et al. 2013; Jumper et al. 2021). In contrast, the CC1NTD has a very low pLDDT score (<50%) because of its disordered nature, as reported previously (Endler et al. 2015). Although there are no known sequence homologs for CC1NTD, the apoplastic domain shares 20% sequence identity with Late Embryogenesis Abundant family 2 (LEA) proteins, LEA14 and LEA2 of Arabidopsis, which are involved in heat and drought stress, supporting a functional role for CC1 in the stress response (Mertens et al. 2018).

CC1NTD structure in solution

Recombinant CC1NTD (1 to 120 aa) was expressed and purified from *Escherichia coli* extracts under nonreducing conditions using Ni-NTA affinity chromatography and size-exclusion chromatography (SEC) as described in the Materials and Methods section (Supplementary Fig. S2A). SEC showed 2 peaks that eluted at 14.8 mL (Peak 1) and 16 mL (Peak 2). Analysis by SDS-PAGE determined that the major species in Peak 1 had a molecular mass of 40 kDa and that in Peak 2 had a molecular mass of 20 kDa, indicating that CC1NTD is present as a monomer–dimer equilibrium (Supplementary Fig. S2C). The CC1NTD dimers were able to be disrupted by the addition of a reducing agent (2 mM tris(2-carboxyethyl)phosphine [TCEP]), which resulted in a single peak by SEC (Supplementary Fig. S2A). A site-specific CC1NTD mutant made by substituting the single cysteine residue (C107) with alanine also resulted in a monomeric protein, demonstrating that dimerization occurs by forming an intermolecular disulfide bond. The CD (Circular Dichroism) spectrum of CC1NTD (Supplementary Fig. S2B) under reducing conditions showed a strong negative ellipticity at about 200 nm, which is similar to the previously reported data (Kesten et al. 2019b). Although the Alphafold2 model does not predict the presence of any secondary structure, CD secondary structure analysis showed that 78% of the protein is disordered and the remaining 22% is beta strands (Supplementary Fig. S2B, Supplementary Table S1) (Micsonai et al. 2015).

We performed size-exclusion chromatography coupled SAXS (SEC–SAXS) to obtain the structural characteristics of the individual species in the monomer–dimer equilibrium purified under nonreducing conditions. For this, ~350 individual SAXS profiles were collected across the SEC elution profile (Fig. 2A). Guinier analysis of each individual profile showed that the R_g values follow a decreasing slope supporting that the sizes of scattering particles decrease with elution volume (Fig. 2A). The data were analyzed using singular value decomposition–evolving factor analysis approach (Meisburger et al. 2016). This approach revealed 2 major species and analysis of the structural parameters obtained from the deconvoluted scattering profiles showed that they represent CC1NTD dimers and monomers (Fig. 2, B and C and Supplementary Fig. S3). Based on Guinier analysis, the CC1NTD monomer has an R_g value of 28.2 ± 0.3 Å, and the pairwise distribution function analysis ($P(r)$) has an extended tail that is characteristic of a disordered protein and an estimated R_g and D_{max} values of 28.4 ± 0.3 and 99 Å. CC1NTD dimers have a slightly increased R_g value of 35.3 ± 0.3 Å and a D_{max} value of 119 Å, obtained from $P(r)$ analysis. The R_g of dimers estimated from Guinier analysis is 33.5 ± 0.4 Å. The details of the structural parameters from the deconvoluted profiles are summarized in Supplementary Tables S2 and S3 (Fig. 2, B and C). The relative amounts of monomer and dimer were calculated from the deconvoluted scattering profiles based on their molecular masses from I_0 (Equation S1; Supplementary Table S2). This yielded a 0.4/0.6 mol fraction of dimer to monomer in the mixture. Kratky analyses showed that the CC1NTD dimer had a partially folded protein conformation, whereas the monomer was fully extended (Supplementary Fig. S4). Other analysis approaches, including

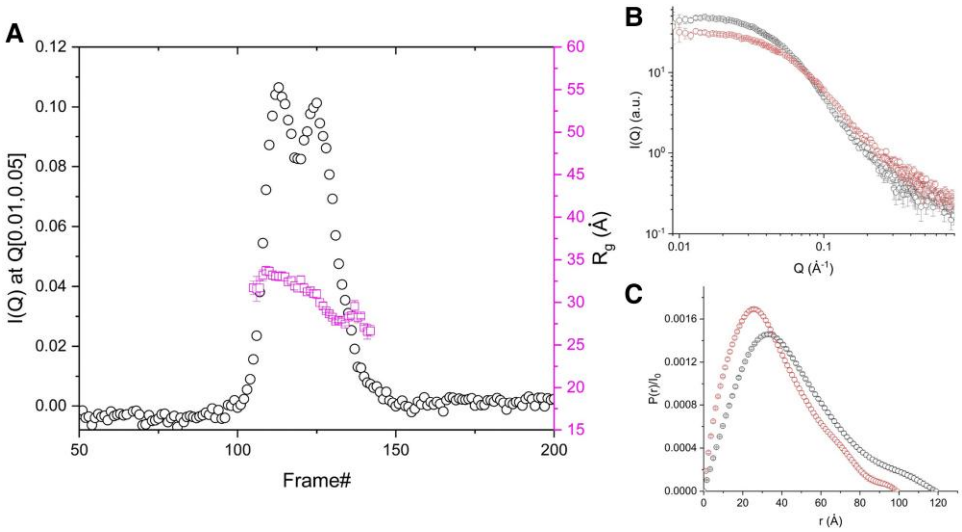

Figure 2. SEC–SAXS of CC1NTD under nonreducing conditions. **A)** The *Y* axis is mean intensity values between the *Q* ranges 0.01 and 0.05 and plotted as open black circles across the frames after buffer subtraction. The R_g distribution (open magenta squares) decreased across the peaks, indicating the presence of a mixture of monomers and dimers. **B)** Deconvoluted SEC–SAXS profiles corresponding to dimers (open black circles) and monomers (open red circles). Uncertainties in SAXS data are shown as solid vertical lines and are derived from counting statistics errors ($N^{½}/N$), where *N* is the number of detector counts. **C)** Pairwise distribution functions of CC1NTD dimers (open black circles) and monomers (open red circles). Errors on *P*(*r*) are standard deviations obtained by propagating the experimental uncertainties in *I*(*Q*) through the indirect Fourier transform.

the polymer physics rule of Flory theory, Ensemble Optimization Method (EOM), and dimensionless Molecular Form Factor (MFF) approach, yielded similar values to those above. Details are provided in Supplementary Fig. S5 and Supplementary Table S3. SEC–SAXS of CC1NTD under reducing conditions (in 2 mM TCEP) and CC1NTD_C107A under nonreducing conditions did not show any evidence of dimers (Supplementary Fig. S6), confirming that the dimerization was through the intermolecular disulfide bond of the single cysteine residue.

Structural analysis of CC1NTD–MT bundles

Paclitaxel-stabilized MTs were formed as described in the Materials and Methods section. Initial characterization of CC1NTD interactions with MTs was carried out with Differential Interference Contrast (DIC) confocal microscopy using a mixture of Alexa488 NHS-labeled CC1NTD and unlabeled CC1NTD at a ratio of 1:4, and paclitaxel-stabilized MTs formed using HiLyte647 labeled tubulin at a ratio of 1:20 with its unlabeled counterpart. The images clearly show that CC1NTD colocalizes with the MTs and provides evidence for the formation of MT bundles (Supplementary Fig. S7). Negative-stain Transmission Electron Microscopy (TEM) showed a random distribution of MTs in the absence of CC1NTD, which changed to a regular arrangement of MTs after mixing with CC1NTD, providing further evidence of CC1NTD associating with MTs to form bundles (Supplementary Fig. S8). In addition, TEM images show that the overall morphology of MTs is cylindrical rod-like particles in the presence and absence of CC1NTD.

We also used SAXS and SANS to characterize the CC1NTD:MTB complexes under reducing conditions. SAXS provided structural information about the MTs alone and the overall structure of the CC1NTD:MTB complex. Using SANS with contrast variation, it was possible to structurally characterize CC1NTD and MTs in the assemblies separately by using partially deuterated CC1NTD ($CC1NTD_D$) to provide contrast with the nondeuterated MTs (Fig. 3). The $CC1NTD_D$:MTB complex was studied in 42% D_2O and 85% D_2O buffers to selectively highlight the scattering contribution from $CC1NTD_D$ and protiated MTs, respectively, while minimizing the scattering contribution from their counterparts.

By combining the structural parameters obtained from SAXS and SANS analysis, we obtained a model of the organization of the CC1NTD:MTB complex. SAXS of free MTs were fitted using a hollow cylinder model, yielding a wall thickness of 47.9 ± 3.2 Å and an inner radius of 84.8 ± 2.0 Å (Fig. 3A), which corresponds to an MT diameter of ~265 Å and is similar to previously reported values (Ojeda-Lopez et al. 2014). The MT length was greater than the spatial range accessed in the SAXS measurements and was not used as a fitting parameter. However, negative-stain TEM (Supplementary Fig. S8) shows they are approximately ~2 μm long, which is consistent with previously reported values for paclitaxel-stabilized MTs (Arnal and Wade 1995). The cross-sectional diameter calculated from the TEM micrographs is roughly 260 Å, consistent with the value we obtained from SAXS.

After adding CC1NTD, SAXS revealed peaks that indicated a more organized arrangement of particles than what we observed with MTs alone (Fig. 3A). As the concentration of CC1NTD was increased, a peak emerged at 0.022 Å^{-1} in the SAXS data along with a series of reflection peaks (Supplementary Fig. S9, Supplementary Table S4). This arrangement followed a consistent spacing between peaks, represented by a ratio of Q_{hk}/Q_{10} of 1: $\sqrt{3}$: $\sqrt{4}$: $\sqrt{7}$: $\sqrt{9}$, which can be interpreted as hexagonal arrays of cylinders. Here, Q_{hk} is the peak center, where hk represents hexagonal indices with Q_{10} marking the first peak at 0.022 Å^{-1}in this sequence, as shown in Fig. 3B (Warren 1941; Alexandridis et al. 1998; Dorin et al. 2012). A squared-Lorentzian function structure factor (Rappolt et al. 2003; Huang et al. 2020) (Equation 1) was used to fit the SAXS data with a CC1NTD-to-tubulin molar ratio of 5.5 (Fig. 3A, Supplementary Table S4).

The SANS profile of $CC1NTD_D$:MTB in 42% D_2O buffer selectively highlights the CC1NTD in the complex and shows peaks at similar positions to the SAXS data. This supports the idea that CC1NTD binds along the surface of the MTs and that it is important for the ordered arrangement of the CC1NTD:MTB complex (Fig. 3C). The primary and secondary peaks at $Q_{10} = 0.022$ Å^{-1}

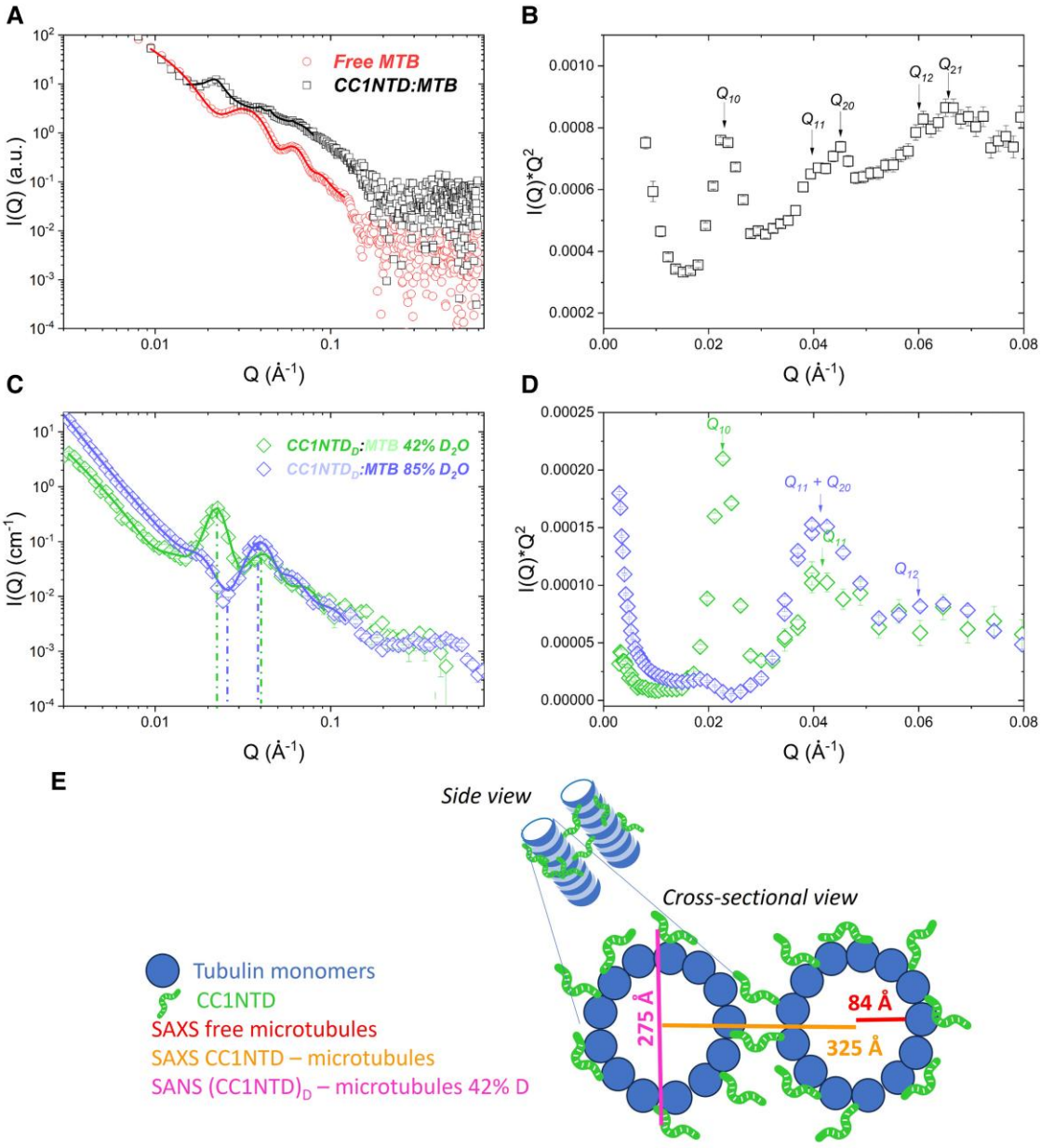

Figure 3. SANS and SAXS of free MTs and the CC1NTD:MTB complex under reducing conditions. **A)** SAXS of free MTs (open red circles) at a tubulin concentration 18 μM (1 mg/mL) and the CC1NTD:MTB complex (18 μM [1 mg/mL]:100 μM [1.5 mg/mL]) shown as open black rectangles. The red line shows the hollow cylinder fit to free MTs, and the black line shows the Lorentzian structure factor fit to the CC1NTD:MTB complex. **B)** Kratky representation of SAXS CC1NTD:MTB data highlighting peak positions of hexagonal array with arrows. **C)** SANS of $CC1NTD_D$:MTB complex in 42% D_2O buffer (open green diamonds; $CC1NTD_D$ at 337 μM [5 mg/mL] and tubulin concentration of 60 μM [3.3 mg/mL]) and 85% D_2O buffer (open blue diamonds; $CC1NTD_D$ at 168 μM [2.5 mg/mL] and tubulin concentration of 30 μM [1.6 mg/mL]) and model fits (green and blue lines). Dashed vertical lines indicate Q_{10} and Q_{11} peak positions discussed in the text. **D)** Kratky representation of SANS $CC1NTD_D$:MTB in 42% and 85% D_2O buffer conditions and peak positions for both data are highlighted by green and blue arrows. **E)** Schematic representation of MTs bundling by CC1NTD based on scattering parameters. CC1NTD monomers (green) interacting with MTs (blue) leads to cross-linking of adjacent MTs. All measurements were under reducing conditions in the presence of 2 mM TCEP. Uncertainties in SAXS and SANS data (Panels **A)** to **D)**) are shown as solid vertical lines and are derived from counting statistics errors ($N^{½}/N$), where N is the number of detector counts.

and $Q_{11} = 0.039$ Å^{-1} are clearly visible in the scattering profiles but because of the low signal-to-noise separation in 42% D_2O buffer higher-order peaks are not well resolved for this neutron contrast condition. In an 85% D_2O buffer, the peak at 0.022 Å^{-1} in the 42% D_2O condition is absent, and instead, presents as a minimum at $Q = 0.0243$ Å^{-1} in the SANS profile. (Fig. 3D). This minimum occurs due to the destructive interference of the scattered neutrons from the protiated MTs and deuterated CC1NTD that have a periodic arrangement in the $CC1NTD_D$:MTB complex (Tainer 2023). The secondary peak at $Q = 0.04$ Å^{-1} becomes prominent in 85% D_2O (Fig. 3D) because it is a superposition of Q_{11} and Q_{20} at 0.038 and 0.0446 Å^{-1}, respectively, which are well resolved in the SAXS data (Fig. 3D and Supplementary Fig. S10). The peaks were fit to a squared Lorentzian function (Equation 1, Table 1) to obtain the peak centers.

We recognize that the hexagonal arrangement of the CC1NTD:MTB complexes is unlikely to reflect the state of the complex in vivo because CC1 is predicted to be a membrane-associated

Table 1. Fitting parameters obtained from fitting SAXS and SANS of the CC1NTD:MTB complexes

Parameter	Peak positions					
Q ($Å^{-1}$)^{SAXS}	0.023	0.040	0.046	0.060	0.065	…
d-spacing[a] (Å)^{SAXS}	274.4	158.3	136.6	104.7	96.7	…
Q ($Å^{-1}$)$^{SANS\ (42\%\ D_2O)}$	0.022	0.041[b]		0.066[b]		…
d-spacing (Å)$^{SANS\ (42\%\ D_2O)}$	281.7	154.1		95.2		…
Q ($Å^{-1}$)$^{SANS\ (85\%\ D_2O)}$	…	0.040[b]		0.058[b]		0.092
d-spacing (Å)$^{SANS\ (85\%\ D_2O)}$	…	158.1		107.4		68.5

[a]Calculated using Equation 2.
[b]The Q-resolution is broad in the SANS data; these peaks were fitted with a single squared Lorentz function, corresponding to the superposition of $Q_{11}+Q_{20}$ and $Q_{20}+Q_{21}$ reflections (Supplementary Fig. S10).

protein (see above). It is more likely that membrane-bound CC1 forms linear arrays of MT bundles in cells (Kesten et al. 2019b). However, the observed hexagonal packing is indicative of a strong association of CC1NTD with the MTs during in vitro studies (Needleman et al. 2004). We calculated the relevant structural parameters of the assembly from SAXS and SANS based on the hexagonal array model (Supplementary Fig. S11). The primary peak position represents an interplanar distance of d_{10} of 277 ± 39 Å in the array, which can be used to determine the center-to-center spacing (a_H) of 325 ± 49 Å of $CC1NTD_D$:MTB complexes, using Equation 2. Since the diameter of free MTs is 265 ± 7 Å, the distance between adjacent MT walls in the assembly is ∼60 Å, indicating a ∼30 Å layer of CC1NTD around the surface of each MT, consistent with the R_g of CC1NTD in solution. We present an overall structural model that shows the spatial dimensions of the arrangement of the CC1NTD with a pair of MTs with CC1NTD forming bridges between MTs to form tightly packed MT arrays (Fig. 3E). These parameters were used as a starting point for the computational analysis described later.

We also compared CC1NTD interactions with MTs under non-reducing conditions to determine if CC1NTD dimerization affects binding. The peak positions in the SANS profiles were the same as in reducing conditions, but the peak intensity was lower (Supplementary Fig. S12). SEC–SAXS showed a 0.4 mol fraction of dimer in the monomer:dimer equilibrium in the absence of a reducing agent, and that the CC1NTD dimer conformation is more compact than the CC1NTD monomer conformation (Table 1). Thus, the disulfide bond in the CC1NTD dimer may affect the accessibility of other residues interacting with MTs, causing CC1NTD dimers to be less likely to interact with MTs. Also, SAXS experiments of CC1NTD_C107A were compared to the wild-type protein under similar concentrations, supporting that C107 is not important for MT binding (Supplementary Fig. S13). In previous work, confocal microscopy imaging of CC1NTD C107 labeled with a maleimide fluorophore did not affect bundling MTs (Kesten et al. 2019b), also supporting that C107 does not prevent MT from bundling.

Molecular interaction dynamics of CC1NTD and MTs

Doubly labeled CC1NTD with an Alexa488 fluorophore attached to the N-terminal amino group and an Alexa594 residue attached to C107 was used to investigate CC1NTD conformations during MT interactions using single-molecule fluorescence (or Förster) resonance energy transfer (smFRET). This construct showed an average FRET efficiency <*E*> of 0.39 ± 0.002 (Fig. 4A) (Equations S7 and S8) after fitting the FRET histogram to a Gaussian function (Fig. 4C). The apparent end-to-end distance, R_{ee}, calculated from <*E*> is 63.8 ± 0.09 Å assuming unbound CC1NTD behaves like a Gaussian coil (Equation S9). These values are comparable to an end-to-end Cα–Cα value of 76.8 Å for CC1NTD monomers obtained from EOM analyses. To infer the R_g from R_{ee} using relation $G = R_{ee}^2/R_g^2$, we again assumed that $G \approx 6$ (a valid assumption for a Gaussian coil-like polymer). The inferred R_g is 25.01 ± 0.05 Å is slightly lower than the SAXS-derived R_g value of ∼28 Å can be attributed to the position of the fluorophore at C107 rather than at the C-terminal residue for smFRET studies. Similarly, from the MFF approach, comparable values of R_{ee} and R_g of CC1NTD monomers fit to SAXS data were obtained (Supplementary Table S3).

Upon MT binding, the <*E*> value decreased to 0.28 ± 0.01 as compared to that with unbound CC1NTD with <*E*> = 0.39 ± 0.002 (Fig. 4B). The apparent R_{ee}, under the same assumptions that CC1NTD behaves like a Gaussian coil, is 66.15 ± 0.05 Å, indicating that CC1NTD has a more extended conformation compared to unbound CC1NTD. Similarly, the calculated R_g is 27 ± 0.02 Å as compared with the unbound CC1NTD value of ∼25 Å. In summary, smFRET shows that CC1NTD has a more extended conformation when bound to MTs with no evidence of it folding into a compact conformation during MT interactions (Fig. 4C). SANS data also show no evidence of compact or folded CC1NTD structures in the presence of MTs. Therefore, we can conclude that CC1NTD retains its disordered conformation and has a large surface accessible area that helps in making fuzzy interactions with MTs to form bundles.

Theoretical model of CC1NTD–MT bundles

The outputs from SAXS, SANS, and smFRET were used to provide the initial structural parameters to guide computational modeling. We built all-atom models of 13 protofilaments and 4 tubulin dimer long (13PF:4) MTs (PDB 3*jal*) (Zhang et al. 2015) and docked CC1NTD conformations to the MTs using LightDock (Jimenez-Garcia et al. 2018; Roel-Touris et al. 2020). As described in the Materials and Methods section, the top conformers were selected for docking to the MT based on the docking score, Y26 distance to the MT, and orientation along the MT long axis (Supplementary Table S5). The CC1NTD:MTB complex was arranged in a single ring hexagonal bundle with a lattice parameter of 322 Å, randomizing the individual CC1NTD:MTB complex at each lattice site. We calculated the SANS profiles for the 42% D_2O and 85% D_2O experimental conditions using Pepsi-SANS (Grudinin et al. 2017) with CC1NTD deuterated to be contrast matched at 85% D_2O (Fig. 5). A workflow of the docking to SANS calculation is shown in Supplementary Fig. S14. The initial model system of 85% D_2O (Fig. 5A) results did not capture the minimum in the experimental results that correspond to the Q_{10} peak found at 0.022 $Å^{-1}$ in 42% D_2O: instead, in the model, there is a peak at the same place. However, the second peak in the calculated 85% data at $Q \sim = 0.039$ $Å^{-1}$ (∼161.1 Å) does correspond with experiments. Thus, the docked conformations (13PF:4-Docked) did not align with the Q_{10}, while the Q_{11} peak is split between 2 shoulders

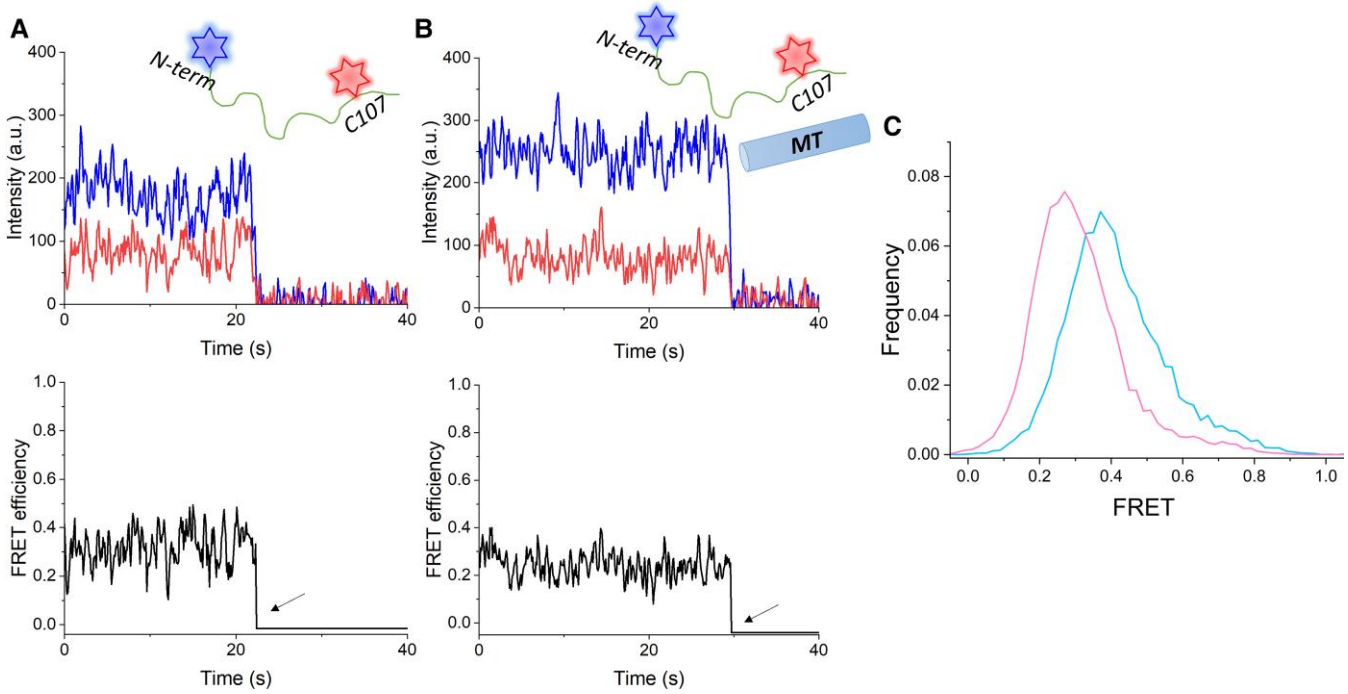

Figure 4. smFRET of CC1NTD labeled with Alexa488 NHS at N-terminus and Alexa594 maleimide at C107, unbound and bound with MTs under reducing conditions. **A)** smFRET traces for unbound CC1NTD and **B)** CC1NTD bound with MTs expressed as fluorescence intensity in arbitrary units (a.u.) vs. time (top graphs). Representative data of a single molecule trace of CC1NTD showing single-step photobleaching with the donor trace in blue and acceptor trace in red and (bottom) corresponding FRET efficiency data of the trace in black; black arrows show the single-step photobleaching; **C)** Comparison of FRET histograms of unbound CC1NTD (blue); $N = 62$ events and CC1NTD during MT interactions (magenta); $N = 82$ events. All measurements were under reducing conditions in the presence of 2 mM TCEP.

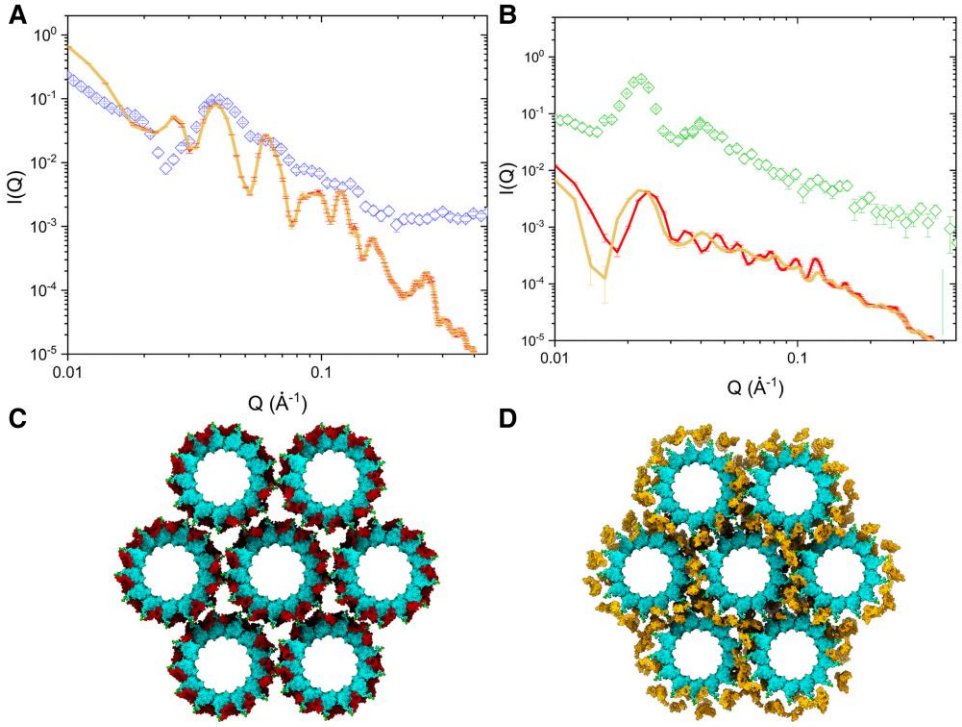

Figure 5. Calculated scattering profiles of the docked and shifted CC1NTD:MTB complexes compared to SANS. **A)** 85% D_2O SANS comparison with the experiment (open blue diamonds), the docked CC1NTD:MTB (red line), and shifted CC1NTD 40 to 45 Å away from the MTB surface (yellow line). **B)** The same as **A)** except calculated for 42% D_2O SANS (open green diamonds). **C)** Example of docked CC1NTD:MTB 13PF:4 complex arranged in the hexagonal lattice. CC1NTD is shown in red. **D)** Example of shifted CC1NTD:MTB 13PF:4 complex arranged in a hexagonal lattice. CC1NTD is shown in yellow. The color of CC1NTD matches the legend in **A)** and **B)**, and MTB is shown in cyan. The solid lines (red/yellow) in **A)** and **B)** are the average scattering profiles from 10 randomized CC1NTD:MTB hexagonal bundles, while the error bars are the standard deviation over the same 10 samples. Uncertainties in SANS data (Panels **A)** and **B)**) are shown as solid vertical lines and are derived from counting statistics errors ($N^{½}/N$), where N is the number of detector counts.

$Q = 0.0360$ Å^{-1} and $Q = 0.0465$ Å^{-1}. These shoulders match the features in the experimental scattering profile.

The Q_{10} peak in the calculated 42% D_2O model gives the lattice parameter, 292 Å, and the calculated Q_{11} peak follows the expected hexagonal packing ratio, indicating that the calculation produced the correct structure factor. However, the position of the Q_{10} peak in the experimental and theoretical curves did not match. Therefore, we hypothesized that the center of mass associated with the deuterated CC1NTD should be centered further away from the MT surface. We tested this by shifting CC1NTD over a range of distances between 15 and 50 Å from the MT surface and found that the best match to the experimental Q_{10} and Q_{11} peaks is obtained when the CC1NTD is between 35 and 45 Å from the surface of the MTs (Supplementary Fig. S15). Although the model Q_{10} and Q_{11} peaks now align with experimental Q_{10} and Q_{11} peaks with a 40 ± 10 Å shift (Fig. 5, B and D), the alignment of the shoulder from the docked structures around the Q_{11} peak is lost ($Q = 0.0465$ Å^{-1}). The agreement of the shoulder from the docked model and the Q_{10}/Q_{11} peak agreement in the shifted ensemble, we hypothesize that the 42% CC1NTD SANS data are best explained by an equilibrium between bound CC1NTD and interstitial CC1NTD between MTBs arranged in the hexagonal assembly.

Discussion

Understanding the structural properties of IDRs and IDPs and how they relate to function continues to be of great interest to the structural biology community because the structure–function paradigm is not understood for these proteins, even though IDRs and IDPs are known to play important roles in a variety of different biological processes (van der Lee et al. 2014). One of the challenges associated with characterizing IDR/IDPs is that traditional structural biology techniques such as protein crystallography, single-particle cryo-electron microscopy, and NMR are not suitable for characterizing these proteins due to their lack of a defined folded structure. This has been addressed by integrating the information from lower-resolution characterization tools such as small-angle scattering, light scattering, smFRET, and analytical ultracentrifugation to extract complementary structural parameters that can be combined with computer modeling and simulation to obtain a molecular model of these systems (Naudi-Fabra et al. 2021).

In this work, we investigated the N-terminal domain of CC1, an IDR, to gain insights into its structure in solution and also when interacting with MTs, where it is proposed to sustain cellulose synthesis by protecting MTs during salt stress. This builds on previous work by Persson and co-workers (Endler et al. 2016; Kesten et al. 2019b), who identified the role of CC1 proteins in maintaining cellulose synthesis and showed the important role of the N-terminal domain in binding to and organizing the MTs under stress conditions. Our motivation was to determine a structural model for the CC1NTD and investigate how its structure may change when it interacts with MTs.

SEC–SAXS revealed that CC1NTD exists as a mixture of monomers and dimers when it is purified under nonreducing conditions. Dimerization is disrupted by the addition of a reducing agent, and we confirmed that the dimerization occurred via C107 through mutation to Ala, which is a monomer. Kratky analysis showed that the dimer has a more compact conformation than the monomer, but that their overall sizes, estimated from D_{max}, are similar. Interestingly, dialysis of a CC1NTD monomer preparation against a buffer solution with no reducing agent resulted in an equilibrium mixture of monomer and dimer similar to that obtained during the nonreducing purification procedure. SANS showed a weaker interaction of the CC1NTD monomer: dimer equilibrium with the MTs, with the inference that the dimer (0.4 mol fraction in the monomer:dimer equilibrium) has a lower affinity for MTs than the monomers (Supplementary Fig. S12). This also suggests that CC1NTD dimerization may restrict its conformation space or prevent critical residues from interacting with MTs. Although the CC1NTD preparation purified under nonreducing conditions provided interesting insights into the CC1NTD conformation, it was not clear if this dimerization was an artifact of the extraction and purification procedure or represents the in cellulo state of this protein. For this reason, we selected to study the protein under reducing conditions, which favored a homogeneous monomer population, for further characterization of its structure alone and when it was interacting with MTs.

Analysis of the monomer using SAXS, smFRET, and CD all indicate a disordered and extended conformation for the protein. CD showed only a small fraction of α-helices and β-sheets, with the majority of the polypeptide chain having a disordered conformation. The EOM analysis of the SAXS data supports an ensemble of conformations that range in R_g and D_{max} values of 30 to 50 and 80 to 150 Å, respectively. The R_g and end-to-end distance values (29 and 72 Å, respectively) obtained from smFRET measurements are comparable to SAXS results, further confirming that CC1NTD is a disordered extended polypeptide chain in solution.

The second goal of our study was to investigate the interaction of the N-terminal domain with MTs. As described above, Persson and co-workers have previously identified CC1 as an MAP and showed that it bundles MTs (Endler et al. 2015; Kesten et al. 2019b). We were interested in understanding this interaction in more detail. Using SANS with contrast variation, it was possible to separate out structural features of CC1NTD from MTs in the complex. Two different contrast conditions were measured using SANS that either selectively highlighted the structure of the bound deuterated CC1NTD (42% D_2O condition) or the protiated MTs (85% D_2O). These measurements were complemented by SAXS characterization of the complex. The addition of CC1NTD to the paclitaxel-stabilized MT preparation resulted in a significant reorganization of the MTs from random hollow cylinders to well-organized MT bundles that were arranged in a hexagonally packed configuration. A similar observation of higher-order bundling of MTs has been reported by SAXS studies of Tau-mediated MT bundling as well as cation-dependent bundling (Needleman et al. 2004; Choi et al. 2009; Chung et al. 2015; Chung et al. 2016).

The contrast-matching SANS experiments revealed 2 important findings. First, the individual scattering profiles of CC1NTD and MTs from SANS in combination with the overall CC1NTD: MTB from SAXS demonstrate that the structure of the complex was dominated by the hexagonal packing of the MT bundles. The second finding was that at the contrast match point for the MTs chosen to selectively highlight the CC1NTD structure, the scattering profile only revealed how CC1NTD is organized in the MT bundles but did not provide structural information about the conformation of individual CC1NTD proteins bound to MTs. This is because the scattering signal was dominated by a regular MT arrangement, which suppressed the signal from the individual CC1NTD proteins. However, smFRET showed that the CC1NTD proteins are in a more extended conformation when bound to the MTs. The combined structure analyses of CC1NTD: MTB show that MTs are efficiently organized into regular arrays by the disordered and extended conformation of CC1NTD. A similar observation was reported for Arabidopsis MAP65-1, which was found to retain its disordered structure during MT interaction,

allowing it to efficiently form cross-bridges between MTs (Gaillard et al. 2008; Tulin et al. 2012).

The structural parameters obtained from the data fitting show that the center-to-center distance between adjacent MTs is 325 Å and the wall-to-wall distance is ∼60 Å. This bundling is significantly more compact than that has been observed in other in vitro studies of MTs (Chang-Jie et al. 1992). NMR established that R23–S30 and Q103–I110 regions interact with MTs (Kesten et al. 2019b). From EOM analysis of the SAXS data, CC1NTD can extend up to 80 Å, which is sufficient to bridge the adjacent MTs based on a wall-to-wall distance of 60 Å (Supplementary Fig. S5, C and D). Computational modeling showed that there are 2 populations of CC1NTD associated with MTs; a bound fraction and a fraction that is unbound but present in the interstitial space between the MTs. This supports a dynamic interaction between CC1NTD that could favor transient bridging between adjacent MTs. It is important to note that the dissociation constant of CC1NTD is ∼10 μM (Endler et al. 2015), which is significantly weaker (∼10 times) than a related MAP, CSI protein-1, which is proposed to facilitate the movement of the CSC in the plasma membrane guided by the cortical MT arrays (Li et al. 2012). A possible reason for this is that disordered MAPs display multivalency in MT interactions, i.e. the presence of multiple binding motifs along their polypeptide chain (Drechsler et al. 2019). This multivalency facilitates weak binding with MTs, also called fuzzy interactions (Tompa and Fuxreiter 2008), in which the disordered MAP retains its disorderliness during interactions. Hence, by retaining a disordered conformation, CC1NTD can make multiple relatively weak interactions along individual MT surfaces and between other proximal MTs, which may help maintain cortical MT arrays under stress conditions. Overall, based on our analysis, we can propose that the CC1NTD remains disordered and retains an extended conformation, which then helps CC1NTD to cross-bridge adjacent MTs. This aligns with an emerging paradigm of MAP MT interactions, which proposes that MAPs can randomly decorate MTs and, through attractive interactions between MAPs, cross-bridge adjacent MTs (Méphon-Gaspard et al. 2016).

In plants, different microscopy studies have reported differences in MT arrangements. For instance, microscopy analyses of paclitaxel-stabilized MT bundles extracted from carrot suspension cells report a center-to-center distance of 340 Å (Cyr and Palevitz 1989), and tobacco (*Nicotiana tabacum*) cell MT extracts in the absence of paclitaxel have 2 populations of MTs with wall-to-wall distances in the range of 120 to 150 and 200 to 250 Å (Chang-Jie et al. 1992). Also, very few MAPs have been characterized during MT interactions. For instance, MAP65 has been identified to cross-link MTs with a wall-to-wall distance of 250 to 300 Å using electron microscopy (Chan et al. 1999), but the molecular-level characterization of plant MAPs remains to be understood. Here, the interactions of CC1NTD with MTs appear very different compared to these other studies; we observe relatively tight binding with MTs. This resembles how human tau interacts with MTs, as described in an earlier study (Kesten et al. 2019b). The structure of tau and how it interacts with MTs have been characterized extensively. (Barbier et al. 2019). Tau has an anionic projection domain that has been identified to control the space between MTs, followed by a proline-rich domain and then the 4 hydrophobic regions known as R repeats (Trinczek et al. 1995). Although there is no sequence homology between tau and CC1NTD, they do share similar structural features, such as the R repeats in tau that have been compared to similar hydrophobic regions in CC1NTD that have been proposed to be the MT interaction sites (Kesten et al. 2019b). NMR (Fung et al. 2020) and smFRET (Melo et al. 2016) studies have shown that tau makes fuzzy interactions with tubulin and retains its disorder during MT interactions, similarly to our present conclusion for CC1NTD. Total internal reflection fluorescence microscopy and cryo-electron microscopy showed that removal of the anionic projection in tau increased the MT bundling efficiency better than the full-length tau, i.e. truncated tau, equivalent to CC1NTD here, bundles MTs into compact arrays (Prezel et al. 2018). Interestingly, the lack of a projection domain in tau (containing only the MT-binding region with 4 Rs) has been shown to bundle MTs more tightly with a wall-to-wall distance of 50 to 60 Å from a SAXS study (Chung et al. 2016), comparable with our observation of CC1NTD-induced MT bundling. Similar to the previous SAXS studies of tau and MTs (Choi et al. 2017), we also observe that CC1NTD increases MT bundling with increasing concentration, and the Q_{10} peak of the hexagonal phase structure factor becomes sharper with increasing concentrations (Supplementary Fig. S9). This indicates that CC1NTD may exhibit a similar behavior to tau and that CC1NTD affects MT structure in a manner that may eventually influence the binding of other MAPs with MTs during stress and modulate cellulose synthesis (Safinya et al. 2019).

Conclusions and future directions

Overall, our SAXS, SANS, smFRET, and modeling data show that CC1NTD has an extended conformation and bundles MTs into compact arrays. The hexagonal arrangement found here may not occur under native conditions because the full-length CC1 is predicted to be a membrane-associated protein, but it shows efficient bundling of MTs by CC1NTD, which may be important for cortical MT assembly during salt stress. We also determined that CC1NTD retains its disordered conformation during MT interactions. This is likely to permit, possibly nonspecific, cross-bridging of MTs so as to maintain cortical MT arrays required for cellulose synthesis. As the current study is limited to only the N-terminal domain, future studies on full-length will provide more insights into how membrane interaction affects MT bundling. While our in vitro results indicate that dimerization of CC1NTD reduces MT bundling, it is possible that oligomerization of full-length CC1 in vivo could enhance its MT association or bundling function. In a cellular context, CC1 may engage in higher-order assemblies through self-interactions or interactions with other proteins. For instance, it has previously been reported that CC1 interacts with CESA proteins, supporting the idea that it plays a role in maintaining CSC function during stress (Endler et al. 2015; Endler et al. 2016). Such oligomerization could promote crosslinking or stabilization of MTs, especially under stress conditions where CC1 is known to support MT organization and cellulose synthesis. Further studies will be needed to determine the oligomeric state of CC1 in vivo and its functional relevance to MT dynamics. CC1 is only one of the members of the CC family of proteins that has been studied so far. Future efforts to compare different CC proteins will shed light on their importance in cellulose synthesis and whether there are any preferential interactions of CCs with different CESAs. In addition, posttranslational modification of MAPs, specifically phosphorylation, affects their structure and possibly their interactions with MTs (Mietelska-Porowska et al. 2014; Ramkumar et al. 2018). Phosphorylation has been identified in many MAPs to dynamically control on/off interactions with MTs (Ramkumar et al. 2018) and can also lead to structural changes in IDPs (Schwalbe et al. 2015). Many phosphoproteomic studies have shown that the CSC and associated proteins are phosphoregulated, including

CC1 (Speicher et al. 2018; Colin et al. 2023). These studies will also determine how posttranslational modifications of CC1 influence its structure and MT interactions.

Materials and methods

Arabidopsis CC1NTD overexpression and purification and formation of MT complexes

Recombinant Arabidopsis (*A. thaliana*) companion of cellulose synthase 1 N-terminal domain (CC1NTD) (1 to 120 aa) and mutant CC1NTD_C107A were over-expressed and purified from *E. coli* BL21(DE3) cultures. Deuterated proteins were produced in a similar manner, except H_2O was substituted for 70% D_2O in the growth media. For purification under reducing conditions, the gel filtration buffer was supplemented with 2 mM TCEP. A detailed description of the expression and purification protocols is provided in Supplementary Text S1. The protocol for circular dichroism analysis is provided in Supplementary Text S2. MTs were prepared using porcine brain tubulin (Cytoskeleton, Inc., T240) in the presence of 2 mM paclitaxel following the manufacturer's protocol. For the formation of a CC1NTD:MTB complex, an MT pellet was first resuspended either in protiated or deuterated general tubulin buffer (80 mM PIPES, 2 mM $MgCl_2$, 0.5 mM EGTA dissolved in H_2O or D_2O, pH 6.9) as required for X-ray or neutron scattering experiments. This was followed by the addition of CC1NTD (1.5 mg/mL, 100 μM) to the polymerized MTs (1 mg/mL tubulin, 18 μM) in a final volume of 100 μL, as previously described (Kesten et al. 2019b). The CC1NTD:MTB mixture was incubated at room temperature for 30 min before measurement.

Small-angle X-ray scattering

SAXS measurements of MTs alone and the CC1NTD:MTB mixture were carried out using a Rigaku BioSAXS-2000 (Rigaku, Tokyo, Japan). The instrument was first calibrated using silver behenate using a configuration with a minimum Q of ~0.008 $Å^{-1}$. Q is defined as $Q = 4\pi \sin\theta/\lambda$, with scattering angle as 2θ and X-ray or neutron wavelength is λ. In total, 24 images were collected during a total of 240 min exposure time for each sample. The raw data were reduced to 1D data using the SAXSLab software package (Rigaku). All images with similar profiles were averaged and buffer subtracted using bioXTAS RAW software (Hopkins et al. 2017) for further analysis. SEC–SAXS of CC1NTD was conducted at the Life Science X-ray Scattering (LiX) beamline of the National Synchrotron Light Source II, Brookhaven National Laboratory, and details of data collection and analysis are presented in detail in Supplementary Text S3.

Small-angle neutron scattering

SANS studies were performed using the Bio-SANS instrument located at the High Flux Isotope Reactor in Oak Ridge National Laboratory (Heller et al. 2014). The instrument was configured with 4 collimation guides in the neutron flight path, the main detector positioned at 7 m from the sample position, and the wing detector positioned at 1.13 m from the sample and rotated to an angle of 3.2° from the direct beam. This configuration has a Q range of $0.007 < Q\ (Å^{-1}) < 0.9$ using 6 Å neutrons with a relative wavelength spread ($\Delta\lambda/\lambda$) of 13.2%. The data were corrected for instrument background, detector sensitivity, and instrument geometry using facility data reduction software, drt-SANS (Heller et al. 2022), using a Python script wrapper. All SANS measurements were performed using cylindrical quartz cuvettes of 1 mm pathlength and 280 μL chamber volume (model 120-000-1-40 Hellma, Müllheim, Germany) at 20 °C.

SAXS and SANS data analysis

CC1NTD solution structures were sampled using the EOM from the ATSAS package (Bernado et al. 2007; Tria et al. 2015). More details can be found in Supplementary Text S3. Free MTs were modeled as homogenous hollow cylinders as described in the Supplementary Text S4. The structure factor for MT bundles was fitted to a squared-Lorentzian function using the following equation:

$$S(q) = c + \frac{2A}{\pi} \times \frac{w}{4(Q - Q_{hk})^2 + w^2} \quad (1)$$

where, $Q_{hk} = Q_{10} \times \sqrt{h^2 + k^2 + hk}$, A is the area of the peak, w is the full width at half maximum, and c is the offset. Here, hk indices refer to 2D hexagonal lattices corresponding to 10, 11, 20, 21, 30, 22, and so on, and Q_{10} is the first peak from a hexagonal lattice. The lattice parameter (a_H) of bundled MTs (Alexandridis et al. 1998) and interplanar d-spacing (d_{10}, d_{11}, so on) is given by the following equation:

$$a_H = \frac{4\pi}{\sqrt{3} \times Q_{10}} = \frac{2 * d_{10}}{\sqrt{3}} = 2 * d_{11} \quad (2)$$

Additional details about SAXS and SANS analysis are provided in Supplementary Text S4.

Fluorescence microscopy

For single-labeled CC1NTD, the primary amine of the N-terminal amino acid of CC1NTD was covalently labeled with Alexa Fluor 488 NHS succinimidyl ester (Invitrogen, USA). For double-labeled CC1NTD, the single cysteine residue C107 was labeled using Alexa Fluor 594 maleimide dye in addition to the N-terminal labeled Alexa Fluor 488. The labeled proteins were immediately flash-frozen using liquid nitrogen and stored at −80 °C until further use. Detailed procedures for the labeling reactions and microscopy measurements are provided in the Supplementary Text S5.

smFRET experiments were carried out using a custom-built prism-based total internal reflection fluorescence microscope based on an inverted IX73 microscope (Olympus) and customized TIRF stage (TIRF Labs Inc., Cary, NC, USA) as described previously (Lamichhane et al. 2010; Baker et al. 2016). 100 pM of doubly labeled CC1NTD with the C-terminal hexa-histidine tag was immobilized onto a biotin-conjugated antihexa-histidine antibody on poly-ethylene glycol passivated quartz microscope slide through biotin–streptavidin interaction in an imaging buffer (20 mM HEPES, 150 mM NaCl, and 2 mM Trolox, pH 8.0). Before imaging, the sample chamber was rinsed using protocatechuic acid/protocatechuate-3,4-dioxygenase oxygen scavenging system to prevent free radical-induced damage of fluorophores (Aitken et al. 2008). The labeled proteins were excited with a 465 nm cable laser (TIRF Labs Inc.). Emission wavelengths were split with a dichroic mirror (T565lpxr-UF2) and were filtered through the filters: ET525/50m and ET605/70m (Chroma Technology Corp.) assembled in a CAIRN cube and Optosplit (CAIRN Research Inc.). The intensities of the donor and acceptor, ID and IA, were detected using an electron-multiplying CCD camera (Andor Technology), which collected data every 100 ms with a gain setting of 300, utilizing a custom single-molecule data acquisition program (Stefanski et al. 2021). Single-molecule time trajectories were obtained using custom scripts written for Interactive Data Language software (Harris Geospatial Solutions Inc., USA). The data acquisition was performed using a program made available by the Ha laboratory (https://github.com/Ha-SingleMoleculeLab). Every molecule was characterized by single-step photobleaching, and the traces were truncated before the photobleaching. All traces were binned to generate histograms. At least 5 independent movies of CC1NTD

only and CC1NTD with MTs were used to generate histograms to estimate standard error values from histograms. Details of the analysis of smFRET data can be found in Supplementary Text S6.

Computational modeling

To determine the localization of CC1NTD with respect to MTs, a *m*PF:*n* CC1NTD:MTB complex was built, where PF stands for protofilament, *m* is the number of protofilaments, and *n* is the number of tubulin dimers in a protofilament. The 3jal PDB (3PF:2) (Zhang et al. 2015) with the EM2-MAP removed was used as the template for the MT, as it gives the correct 13 PF MT used in the experiments. The 3PF:2 structure was replicated longitudinally and rotationally to form a full 13PF:4 MT by aligning the terminal dimer or protofilament with the first dimer/protofilament. The individual tubulin monomers, GTP, and Mg^{2+} ions were saved to separate PDB files. One thousand CC1NTD monomers were generated using the EOM (Bernado et al. 2007; Tria et al. 2015), which produced coarse-grained random coils with the monomer SEC–SAXS data as constraints. These were converted to all-atom models, energy minimized, and refined to 30 structures (see Supplementary Text S7 for details). The 30 conformers were docked to a 3PF:4 MT patch with LightDock (Jimenez-Garcia et al. 2018; Roel-Touris et al. 2020), a protein–protein docking software that uses a glowworm swarm optimization algorithm to optimize binding poses of proteins according to a docking score (fastDFIRE) (Zhang et al. 2005), with 30 swarms and 100 structures per swarm. We applied the cross-linked mass spectrometry data (Kesten et al. 2019b) as active restraints, i.e. the restraints contribute to the scoring during docking. We restrained E111:E158 on the β-tubulin as the receptor and K40/K94/K96 on CC1NTD as the ligands. Nineteen docked poses (Supplementary Table S5) were selected from the pool of 90,000 poses for building the CC1NTD:MTB complex (see Supplementary Text S7 for further details).

The CC1NTD:MTB complex was built with *psfgen* in VMD (Humphrey et al. 1996) by aligning the 3PF:4 MT patch with the docked CC1NTD monomer to a β-tubulin on the 13PF:*n* MT. During this step, a CC1NTD conformer was randomly selected from the set of top-ranked poses and positioned along the PF. This was repeated over the full 13PF:4 MT until all dimers had one CC1NTD bound. Subsequently, the CC1NTD:MTB complexes were bundled into a specific geometry by loading a random set of CC1NTD:MTB complexes and moving them to the necessary lattice sites with a provided lattice parameter. The final bundled complex was saved as a *dcd* trajectory file, then concatenated into a single pdb with *mdtraj* (McGibbon et al. 2015) to calculate the SANS profiles using *Pepsi-SANS* (Grudinin et al. 2017). In this study, 10 hexagonal CC1NTD:MTB bundles were generated from 20 CC1NTD:MTB (13PF:4) complexes with a lattice parameter of 322 ± 10 Å for 2 conditions, keeping the docked structures (Docked) and shifting the CC1NTD perpendicularly from the surface by 40 ± 10 Å (Shifted). Small-angle scattering profiles were calculated using *Pepsi-SAXS/SANS* (Grudinin et al. 2017) from 0.0 to 0.5 $Å^{-1}$ with 250 data points and out to the 75th order in the multipole expansion. CC1NTD was 51% deuterated at the nonexchangeable sites to match the protein at 85% D_2O. A complete workflow is shown in Supplementary Fig. S14. Further analysis was performed with in-house Python scripts and plotted using *seaborn* and/or *matplotlib* in Python.

Accession numbers

Sequence data for Arabidopsis CC1 used in this article can be found in the GenBank/EMBL data libraries under accession number Q9C636.

Acknowledgments

This research used resources at the High Flux Isotope Reactor and Spallation Neutron Source, a DOE Office of Science User Facility operated by the Oak Ridge National Laboratory. This research used resources of the Compute and Data Environment for Science (CADES) at the Oak Ridge National Laboratory, which is supported by the Office of Science of the U.S. Department of Energy under Contract No. DE-AC05-00OR22725. The authors thank Dr Volker Urban and Dr Sai Venkatesh Pingali for discussions about SANS data interpretation. Additionally, they thank Dr Kevin Weiss and Ms Qiu Zhang for advice and support in producing protiated and deuterated CC1NTD used in this study.

Author contributions

V.G. prepared samples for analysis, performed all experimental work, and associated data analysis. W.C.L. planned and performed SANS experiments and data analysis. S.C. performed SEC SAXS measurements at the LiX beamline. R.L., S.T.K., and J.L.K. performed fluorescence and electron microscopy experiments. J.C.S. and A.C.H. designed and performed computational modeling. H.O. directed the research project. V.G. and H.O. wrote the manuscript with input from all authors. All authors had the opportunity to read and comment on the manuscript.

Supplementary data

The following materials are available in the online version of this article.

Supplementary Figure S1. Bioinformatic analyses of Arabidopsis CC1NTD

Supplementary Figure S2. SEC of CC1NTD under nonreducing and reducing conditions.

Supplementary Figure S3. Single value decomposition analysis of CC1NTD SEC–SAXS data under nonreducing conditions.

Supplementary Figure S4. Kratky representation of CC1NTD dimer and monomer after deconvolution of SEC–SAXS data

Supplementary Figure S5. Analysis of CC1NTD monomers obtained from SEC–SAXS using the EOM

Supplementary Figure S6. Comparison of SEC–SAXS of CC1NTD and CC1NTD_C107A mutant

Supplementary Figure S7. Confocal microscopy shows colocalization of CC1NTD and MTs

Supplementary Figure S8. TEM of MT bundling in the presence of CC1NTD

Supplementary Figure S9. SAXS of CC1NTD–MT mixture at increasing concentrations of CC1NTD

Supplementary Figure S10. Analysis of peak positions in SANS of CC1NTD-MT complex in 85% D_2O

Supplementary Figure S11. Schematic representation of scattering planes of CC1NTD–MT hexagonal arrays

Supplementary Figure S12. Comparison of $CC1NTD_D$–MT complex under reducing and nonreducing conditions

Supplementary Figure S13. Comparison of CC1NTD and CC1NTD_C107A MT complexes

Supplementary Figure S14. Workflow for generating the CC1NTD–MT complexes and analysis approach

Supplementary Figure S15. Effect of changing CC1NTD position relative to MTs on peak positions in theoretical SANS curves.

Supplementary Table S1. Secondary structure analysis of CC1NTD

Supplementary Table S2. Summary of structural parameters from deconvoluted profiles of SEC–SAXS of CC1NTD under nonreducing conditions

Supplementary Table S3. Summary of structural parameters of CC1NTD from SAXS and modeling

Supplementary Table S4. Structural parameters of fitting CC1NTD–MT bundles fitted to the hollow cylinder model and Lorentzian structure factor

Supplementary Table S5. CC1NTD conformers selected for creating CC1NTD–MT complexes after the refinement of the docking poses

Supplementary Text S1. Protein preparation and characterization

Supplementary Text S2. Physicochemical characterization of CC1NTD

Supplementary Text S3. SAXS analysis of CC1NTD

Supplementary Text S4. Characterization of CC1NTD–MT complexes with SAXS and SANS

Supplementary Text S5. Microscopy of CC1NTD–MT complexes

Supplementary Text S6. smFRET experiments

Supplementary Text S7. Computational modeling of CC1NTD–MT complex

Funding

V.G. and H.O. acknowledge funding by the Center for Lignocellulose Structure and Formation supported by the U.S. Department of Energy (DOE), Office of Science, Basic Energy Sciences under Award # DE-SC0001090. A.C.H. and J.C.S. acknowledge support of the project ERKPA14 funded by the DOE Office of Biological & Environmental Research (OBER) for computational modeling. W.C.L. supported SANS experiments on Bio-SANS, which is part of the Center for Structural Molecular Biology, funded by DOE OBER project ERKP291. S.C. supported SAXS experiments on the LiX beamline, which is part of the Center for BioMolecular Structure (CBMS), funded by the National Institutes of Health, National Institute of General Medical Sciences (NIGMS) through a P30 Grant (P30GM133893), and by the DOE Office of Biological and Environmental Research (KP1605010). LiX also received additional support from NIH Grant S10 OD012331. RL acknowledges support from the National Institutes of Health R35GM142946 and the start-up funds from the College of Arts and Sciences, University of Tennessee, Knoxville, for fluorescence microscopy work.

Conflict of interest statement. None declared.

Data availability

The data underlying this article will be shared on reasonable request to the corresponding author.

References

Aitken CE, Marshall RA, Puglisi JD. An oxygen scavenging system for improvement of dye stability in single-molecule fluorescence experiments. *Biophys J*. 2008:94(5):1826–1835. https://doi.org/10.1529/biophysj.107.117689

Albrecht V, Šimková K, Carrie C, Delannoy E, Giraud E, Whelan J, Small ID, Apel K, Badger MR, Pogson BJ. The cytoskeleton and the peroxisomal-targeted snowy cotyledon3 protein are required for chloroplast development in *Arabidopsis*. *Plant Cell*. 2010:22(10):3423–3438. https://doi.org/10.1105/tpc.110.074781

Alexandridis P, Olsson U, Lindman B. A record nine different phases (four cubic, two hexagonal, and one lamellar lyotropic liquid crystalline and two micellar solutions) in a ternary isothermal system of an amphiphilic block copolymer and selective solvents (water and oil). *Langmuir*. 1998:14(10):2627–2638. https://doi.org/10.1021/la971117c

Arendt T, Stieler JT, Holzer M. Tau and tauopathies. *Brain Res Bull*. 2016:126:238–292. https://doi.org/10.1016/j.brainresbull.2016.08.018

Arnal I, Wade RH. How does taxol stabilize microtubules? *Curr Biol*. 1995:5(8):900–908. https://doi.org/10.1016/S0960-9822(95)00180-1

Baker KA, Lamichhane R, Lamichhane T, Rueda D, Cunningham PR. Protein-RNA dynamics in the central junction control 30S ribosome assembly. *J Mol Biol*. 2016:428(18):3615–3631. https://doi.org/10.1016/j.jmb.2016.05.010

Barbier P, Zejneli O, Martinho M, Lasorsa A, Belle V, Smet-Nocca C, Tsvetkov PO, Devred F, Landrieu I. Role of tau as a microtubule-associated protein: structural and functional aspects. *Front Aging Neurosci*. 2019:11:204. https://doi.org/10.3389/fnagi.2019.00204

Bernado P, Mylonas E, Petoukhov MV, Blackledge M, Svergun DI. Structural characterization of flexible proteins using small-angle X-ray scattering. *J Am Chem Soc*. 2007:129(17):5656–5664. https://doi.org/10.1021/ja069124n

Bodakuntla S, Jijumon AS, Villablanca C, Gonzalez-Billault C, Janke C. Microtubule-associated proteins: structuring the cytoskeleton. *Trends Cell Biol*. 2019:29(10):804–819. https://doi.org/10.1016/j.tcb.2019.07.004

Brouhard GJ, Rice LM. Microtubule dynamics: an interplay of biochemistry and mechanics. *Nat Rev Mol Cell Biol*. 2018:19(7):451–463. https://doi.org/10.1038/s41580-018-0009-y

Chan J, Jensen CG, Jensen LC, Bush M, Lloyd CW. The 65-kDa carrot microtubule-associated protein forms regularly arranged filamentous cross-bridges between microtubules. *Proc Natl Acad Sci U S A*. 1999:96(26):14931–14936. https://doi.org/10.1073/pnas.96.26.14931

Chang-Jie J, Sonobe S, Shibaoka H. Assembly of microtubules in a cytoplasmic extract of tobacco BY-2 miniprotoplasts in the absence of microtubule-stabilizing agents. *Plant Cell Physiol*. 1992:33:497–501. https://doi.org/10.1093/oxfordjournals.pcp.a078281

Choi MC, Chung PJ, Song C, Miller HP, Kiris E, Li Y, Wilson L, Feinstein SC, Safinya CR. Paclitaxel suppresses tau-mediated microtubule bundling in a concentration-dependent manner. *Biochim Biophys Acta Gen Subj*. 2017:1861(1):3456–3463. https://doi.org/10.1016/j.bbagen.2016.09.011

Choi MC, Raviv U, Miller HP, Gaylord MR, Kiris E, Ventimiglia D, Needleman DJ, Kim MW, Wilson L, Feinstein SC, *et al.* Human microtubule-associated-protein tau regulates the number of protofilaments in microtubules: a synchrotron X-ray scattering study. *Biophys J*. 2009:97(2):519–527. https://doi.org/10.1016/j.bpj.2009.04.047

Chung PJ, Choi MC, Miller HP, Feinstein HE, Raviv U, Li Y, Wilson L, Feinstein SC, Safinya CR. Direct force measurements reveal that protein tau confers short-range attractions and isoform-dependent steric stabilization to microtubules. *Proc Natl Acad Sci U S A*. 2015:112(47):E6416–E6425. https://doi.org/10.1073/pnas.1513172112

Chung PJ, Song C, Deek J, Miller HP, Li Y, Choi MC, Wilson L, Feinstein SC, Safinya CR. Tau mediates microtubule bundle architectures mimicking fascicles of microtubules found in the axon initial segment. *Nat Commun*. 2016:7(1):12278. https://doi.org/10.1038/ncomms12278

Colin L, Ruhnow F, Zhu JK, Zhao C, Zhao Y, Persson S. The cell biology of primary cell walls during salt stress. *Plant Cell*. 2023:35(1): 201–217. https://doi.org/10.1093/plcell/koac292

Cyr RJ, Palevitz BA. Microtubule-binding proteins from carrot: I. Initial characterization and microtubule bundling. *Planta*. 1989:177(2):245–260. https://doi.org/10.1007/BF00392813

Dixit R, Cyr R. The cortical microtubule array: from dynamics to organization. *Plant Cell*. 2004:16(10):2546–2552. https://doi.org/10.1105/tpc.104.161030

Dobson L, Remenyi I, Tusnady GE. CCTOP: a consensus constrained TOPology prediction web server. *Nucleic Acids Res*. 2015:43(W1): W408–W412. https://doi.org/10.1093/nar/gkv451

Dorin RM, Marques DS, Sai H, Vainio U, Phillip WA, Peinemann KV, Nunes SP, Wiesner U. Solution small-angle X-ray scattering as a screening and predictive tool in the fabrication of asymmetric block copolymer membranes. *ACS Macro Lett*. 2012:1(5):614–617. https://doi.org/10.1021/mz300100b

Drechsler H, Xu Y, Geyer VF, Zhang Y, Diez S. Multivalent electrostatic microtubule interactions of synthetic peptides are sufficient to mimic advanced MAP-like behavior. *Mol Biol Cell*. 2019:30(24):2953–2968. https://doi.org/10.1091/mbc.E19-05-0247

Elliott A, Shaw SL. Update: plant cortical microtubule arrays. *Plant Physiol*. 2018:176(1):94–105. https://doi.org/10.1104/pp.17.01329

Endler A, Kesten C, Schneider R, Zhang Y, Ivakov A, Froehlich A, Funke N, Persson S. A mechanism for sustained cellulose synthesis during salt stress. *Cell*. 2015:162(6):1353–1364. https://doi.org/10.1016/j.cell.2015.08.028

Endler A, Schneider R, Kesten C, Lampugnani ER, Persson S. The cellulose synthase companion proteins act non-redundantly with CELLULOSE SYNTHASE INTERACTING1/POM2 and CELLULOSE SYNTHASE 6. *Plant Signal Behav*. 2016:11(4):e1135281. https://doi.org/10.1080/15592324.2015.1135281

Fung HYJ, McKibben KM, Ramirez J, Gupta K, Rhoades E. Structural characterization of tau in fuzzy tau:tubulin complexes. *Structure*. 2020:28(3):378–384.e4. https://doi.org/10.1016/j.str.2020.01.004

Gaillard J, Neumann E, Van Damme D, Stoppin-Mellet V, Ebel C, Barbier E, Geelen D, Vantard M. Two microtubule-associated proteins of *Arabidopsis* MAP65s promote antiparallel microtubule bundling. *Mol Biol Cell*. 2008:19(10):4534–4544. https://doi.org/10.1091/mbc.e08-04-0341

Gardiner J. The evolution and diversification of plant microtubule-associated proteins. *Plant J*. 2013:75(2):219–229. https://doi.org/10.1111/tpj.12189

Gonzalez JP, Frandsen KEH, Kesten C. The role of intrinsic disorder in binding of plant microtubule-associated proteins to the cytoskeleton. *Cytoskeleton (Hoboken)*. 2023:80(11-12):404–436. https://doi.org/10.1002/cm.21773

Goodson HV, Jonasson EM. Microtubules and microtubule-associated proteins. *Cold Spring Harb Perspect Biol*. 2018:10(6): a022608. https://doi.org/10.1101/cshperspect.a022608

Green PB. Organogenesis-a biophysical view. *Annu Rev Plant Physiol*. 1980:31(1):51–82. https://doi.org/10.1146/annurev.pp.31.060180.000411

Grudinin S, Garkavenko M, Kazennov A. *Pepsi-SAXS*: an adaptive method for rapid and accurate computation of small-angle X-ray scattering profiles. *Acta Crystallogr D Struct Biol*. 2017:73(5): 449–464. https://doi.org/10.1107/S2059798317005745

Gu Y, Kaplinsky N, Bringmann M, Cobb A, Carroll A, Sampathkumar A, Baskin TI, Persson S, Somerville CR. Identification of a cellulose synthase-associated protein required for cellulose biosynthesis. *Proc Natl Acad Sci U S A*. 2010:107(29):12866–12871. https://doi.org/10.1073/pnas.1007092107

Guharoy M, Szabo B, Contreras Martos S, Kosol S, Tompa P. Intrinsic structural disorder in cytoskeletal proteins. *Cytoskeleton (Hoboken)*. 2013:70(10):550–571. https://doi.org/10.1002/cm.21118

Hashimoto T. Microtubules in plants. *Arabidopsis Book*. 2015:13: e0179. https://doi.org/10.1199/tab.0179

Heller WT, Hetrick J, Bilheux J, Calvo JMB, Chen W-R, DeBeer-Schmitt L, Do C, Doucet M, Fitzsimmons MR, Godoy WF. Drtsans: the data reduction toolkit for small-angle neutron scattering at Oak Ridge National Laboratory. *SoftwareX*. 2022:19:101101. https://doi.org/10.1016/j.softx.2022.101101

Heller WT, Urban VS, Lynn GW, Weiss KL, O'Neill HM, Pingali SV, Qian S, Littrell KC, Melnichenko YB, Buchanan MV. The Bio-SANS instrument at the high flux isotope reactor of Oak Ridge National Laboratory. *J Appl Crystallogr*. 2014:47(4): 1238–1246. https://doi.org/10.1107/S1600576714011285

Hopkins JB, Gillilan RE, Skou S. *BioXTAS RAW*: improvements to a free open-source program for small-angle X-ray scattering data reduction and analysis. *J Appl Crystallogr*. 2017:50(5):1545–1553. https://doi.org/10.1107/S1600576717011438

Huang N, Tao J, Wei S, Huang W, Wang D. Positional order in the columnar phase of lyotropic chromonic liquid crystals mediated by ionic additives. *ACS Omega*. 2020:5(17):9937–9943. https://doi.org/10.1021/acsomega.0c00229

Humphrey W, Dalke A, Schulten K. VMD: visual molecular dynamics. *J Mol Graph*. 1996:14(1):33–38. https://doi.org/10.1016/0263-7855(96)00018-5

Jimenez-Garcia B, Roel-Touris J, Romero-Durana M, Vidal M, Jimenez-Gonzalez D, Fernandez-Recio J. LightDock: a new multi-scale approach to protein-protein docking. *Bioinformatics*. 2018:34(1):49–55. https://doi.org/10.1093/bioinformatics/btx555

Jumper J, Evans R, Pritzel A, Green T, Figurnov M, Ronneberger O, Tunyasuvunakool K, Bates R, Zidek A, Potapenko A, *et al*. Highly accurate protein structure prediction with AlphaFold. *Nature*. 2021:596(7873):583–589. https://doi.org/10.1038/s41586-021-03819-2

Kesten C, Gamez-Arjona FM, Menna A, Scholl S, Dora S, Huerta AI, Huang HY, Tintor N, Kinoshita T, Rep M, *et al*. Pathogen-induced pH changes regulate the growth-defense balance in plants. *EMBO J*. 2019a:38(24):e101822. https://doi.org/10.15252/embj.2019101822

Kesten C, Wallmann A, Schneider R, McFarlane HE, Diehl A, Khan GA, van Rossum BJ, Lampugnani ER, Szymanski WG, Cremer N, *et al*. The companion of cellulose synthase 1 confers salt tolerance through a tau-like mechanism in plants. *Nat Commun*. 2019b:10(1):857. https://doi.org/10.1038/s41467-019-08780-3

Lamichhane R, Solem A, Black W, Rueda D. Single-molecule FRET of protein-nucleic acid and protein-protein complexes: surface passivation and immobilization. *Methods*. 2010:52(2):192–200. https://doi.org/10.1016/j.ymeth.2010.06.010

Lei L, Li S, Bashline L, Gu Y. Dissecting the molecular mechanism underlying the intimate relationship between cellulose microfibrils and cortical microtubules. *Front Plant Sci*. 2014:5:90. https://doi.org/10.3389/fpls.2014.00090

Li H, Mao T, Zhang Z, Yuan M. The AtMAP65-1 cross-bridge between microtubules is formed by one dimer. *Plant Cell Physiol*. 2007:48(6): 866–874. https://doi.org/10.1093/pcp/pcm059

Li S, Lei L, Somerville CR, Gu Y. Cellulose synthase interactive protein 1 (CSI1) links microtubules and cellulose synthase complexes. *Proc Natl Acad Sci U S A*. 2012:109(1):185–190. https://doi.org/10.1073/pnas.1118560109

Lucas JR, Courtney S, Hassfurder M, Dhingra S, Bryant A, Shaw SL. Microtubule-associated proteins MAP65-1 and MAP65-2 positively regulate axial cell growth in etiolated *Arabidopsis*

hypocotyls. *Plant Cell*. 2011:23(5):1889–1903. https://doi.org/10.1105/tpc.111.084970

Ma H, Xu L, Fu Y, Zhu L. Arabidopsis QWRF1 and QWRF2 redundantly modulate cortical microtubule arrangement in floral organ growth and fertility. *Front Cell Dev Biol*. 2021:9:634218. https://doi.org/10.3389/fcell.2021.634218

Mariani V, Biasini M, Barbato A, Schwede T. lDDT: a local superposition-free score for comparing protein structures and models using distance difference tests. *Bioinformatics*. 2013:29(21):2722–2728. https://doi.org/10.1093/bioinformatics/btt473

McGibbon RT, Beauchamp KA, Harrigan MP, Klein C, Swails JM, Hernandez CX, Schwantes CR, Wang LP, Lane TJ, Pande VS. MDTraj: a modern open library for the analysis of molecular dynamics trajectories. *Biophys J*. 2015:109(8):1528–1532. https://doi.org/10.1016/j.bpj.2015.08.015

Meisburger SP, Taylor AB, Khan CA, Zhang S, Fitzpatrick PF, Ando N. Domain movements upon activation of phenylalanine hydroxylase characterized by crystallography and chromatography-coupled small-angle X-ray scattering. *J Am Chem Soc*. 2016:138(20):6506–6516. https://doi.org/10.1021/jacs.6b01563

Melo AM, Coraor J, Alpha-Cobb G, Elbaum-Garfinkle S, Nath A, Rhoades E. A functional role for intrinsic disorder in the tau-tubulin complex. *Proc Natl Acad Sci U S A*. 2016:113(50):14336–14341. https://doi.org/10.1073/pnas.1610137113

Méphon-Gaspard A, Boca M, Pioche-Durieu C, Desforges B, Burgo A, Hamon L, Piétrement O, Pastré D. Role of tau in the spatial organization of axonal microtubules: keeping parallel microtubules evenly distributed despite macromolecular crowding. *Cell Mol Life Sci*. 2016:73(19):3745–3760. https://doi.org/10.1007/s00018-016-2216-z

Mertens J, Aliyu H, Cowan DA. LEA proteins and the evolution of the WHy domain. *Appl Environ Microbiol*. 2018:84:e00539-18. https://doi.org/10.1128/AEM.00539-18

Micsonai A, Wien F, Kernya L, Lee Y-H, Goto Y, Réfrégiers M, KardosJ. Accurate secondary structure prediction and fold recognition for circular dichroism spectroscopy. *Proc Natl Acad Sci U S A*. 2015:112(24):E3095–E3103. https://doi.org/10.1073/pnas.1500851112

Mietelska-Porowska A, Wasik U, Goras M, Filipek A, Niewiadomska G. Tau protein modifications and interactions: their role in function and dysfunction. *Int J Mol Sci*. 2014:15(3):4671–4713. https://doi.org/10.3390/ijms15034671

Morris M, Maeda S, Vossel K, Mucke L. The many faces of tau. *Neuron*. 2011:70(3):410–426. https://doi.org/10.1016/j.neuron.2011.04.009

Naudi-Fabra S, Tengo M, Jensen MR, Blackledge M, Milles S. Quantitative description of intrinsically disordered proteins using single-molecule FRET, NMR, and SAXS. *J Am Chem Soc*. 2021:143(48):20109–20121. https://doi.org/10.1021/jacs.1c06264

Needleman DJ, Ojeda-Lopez MA, Raviv U, Miller HP, Wilson L, Safinya CR. Higher-order assembly of microtubules by counterions: from hexagonal bundles to living necklaces. *Proc Natl Acad Sci U S A*. 2004:101(46):16099–16103. https://doi.org/10.1073/pnas.0406076101

Ojeda-Lopez MA, Needleman DJ, Song C, Ginsburg A, Kohl PA, Li Y, Miller HP, Wilson L, Raviv U, Choi MC, *et al.* Transformation of taxol-stabilized microtubules into inverted tubulin tubules triggered by a tubulin conformation switch. *Nat Mater*. 2014:13(2):195–203. https://doi.org/10.1038/nmat3858

Pignocchi C, Minns GE, Nesi N, Koumproglou R, Kitsios G, Benning C, Lloyd CW, Doonan JH, Hills MJ. ENDOSPERM DEFECTIVE1 is a novel microtubule-associated protein essential for seed development in *Arabidopsis*. *Plant Cell*. 2009:21(1):90–105. https://doi.org/10.1105/tpc.108.061812

Prezel E, Elie A, Delaroche J, Stoppin-Mellet V, Bosc C, Serre L, Fourest-Lieuvin A, Andrieux A, Vantard M, Arnal I. Tau can switch microtubule network organizations: from random networks to dynamic and stable bundles. *Mol Biol Cell*. 2018:29(2):154–165. https://doi.org/10.1091/mbc.E17-06-0429

Ramkumar A, Jong BY, Ori-McKenney KM. ReMAPping the microtubule landscape: how phosphorylation dictates the activities of microtubule-associated proteins. *Dev Dyn*. 2018:247(1):138–155. https://doi.org/10.1002/dvdy.24599

Rappolt M, Hickel A, Bringezu F, Lohner K. Mechanism of the lamellar/inverse hexagonal phase transition examined by high resolution x-ray diffraction. *Biophys J*. 2003:84(5):3111–3122. https://doi.org/10.1016/S0006-3495(03)70036-8

Roel-Touris J, Bonvin A, Jimenez-Garcia B. LightDock goes information-driven. *Bioinformatics*. 2020:36(3):950–952. https://doi.org/10.1093/bioinformatics/btz642

Safinya CR, Chung PJ, Song C, Li Y, Miller HP, Choi MC, Raviv U, Ewert KK, Wilson L, Feinstein SC. Minireview—microtubules and tubulin oligomers: shape transitions and assembly by intrinsically disordered protein tau and cationic biomolecules. *Langmuir*. 2019:35(48):15970–15978. https://doi.org/10.1021/acs.langmuir.9b02208

Sasabe M, Soyano T, Takahashi Y, Sonobe S, Igarashi H, Itoh TJ, Hidaka M, Machida Y. Phosphorylation of NtMAP65-1 by a MAP kinase down-regulates its activity of microtubule bundling and stimulates progression of cytokinesis of tobacco cells. *Genes Dev*. 2006:20(8):1004–1014. https://doi.org/10.1101/gad.1408106

Schwalbe M, Kadavath H, Biernat J, Ozenne V, Blackledge M, Mandelkow E, Zweckstetter M. Structural impact of tau phosphorylation at threonine 231. *Structure*. 2015:23(8):1448–1458. https://doi.org/10.1016/j.str.2015.06.002

Smertenko AP, Chang H-Y, Sonobe S, Fenyk SI, Weingartner M, Bögre L, Hussey PJ. Control of the AtMAP65-1 interaction with microtubules through the cell cycle. *J Cell Sci*. 2006:119(15):3227–3237. https://doi.org/10.1242/jcs.03051

Speicher TL, Li PZ, Wallace IS. Phosphoregulation of the plant cellulose synthase complex and cellulose synthase-like proteins. *Plants (Basel)*. 2018:7(3):52. https://doi.org/10.3390/plants7030052

Stefanski KM, Russell CM, Westerfield JM, Lamichhane R, Barrera FN. PIP(2) promotes conformation-specific dimerization of the EphA2 membrane region. *J Biol Chem*. 2021:296:100149. https://doi.org/10.1074/jbc.RA120.016423

Tainer J. *Scattering methods in structural biology*. *Part B*. Volume 678. Cambridge, MA: Academic Press; 2023.

Tompa P, Fuxreiter M. Fuzzy complexes: polymorphism and structural disorder in protein-protein interactions. *Trends Biochem Sci*. 2008:33(1):2–8. https://doi.org/10.1016/j.tibs.2007.10.003

Tria G, Mertens HD, Kachala M, Svergun DI. Advanced ensemble modelling of flexible macromolecules using X-ray solution scattering. *IUCrJ*. 2015:2(2):207–217. https://doi.org/10.1107/S205225251500202X

Trinczek B, Biernat J, Baumann K, Mandelkow EM, Mandelkow E. Domains of tau protein, differential phosphorylation, and dynamic instability of microtubules. *Mol Biol Cell*. 1995:6(12):1887–1902. https://doi.org/10.1091/mbc.6.12.1887

Tulin A, McClerklin S, Huang Y, Dixit R. Single-molecule analysis of the microtubule cross-linking protein MAP65-1 reveals a molecular mechanism for contact-angle-dependent microtubule bundling. *Biophys J*. 2012:102(4):802–809. https://doi.org/10.1016/j.bpj.2012.01.008

van der Lee R, Buljan M, Lang B, Weatheritt RJ, Daughdrill GW, Dunker AK, Fuxreiter M, Gough J, Gsponer J, Jones DT, *et al.*

Classification of intrinsically disordered regions and proteins. *Chem Rev*. 2014:114(13):6589–6631. https://doi.org/10.1021/cr400525m

Varadi M, Anyango S, Deshpande M, Nair S, Natassia C, Yordanova G, Yuan D, Stroe O, Wood G, Laydon A, *et al*. AlphaFold protein structure database: massively expanding the structural coverage of protein-sequence space with high-accuracy models. *Nucleic Acids Res*. 2022:50(D1):D439–D444. https://doi.org/10.1093/nar/gkab1061

Warren B. X-ray diffraction in random layer lattices. *Phys Rev*. 1941:59(9):693–698. https://doi.org/10.1103/PhysRev.59.693

Wen HL, Lin YT, Ting CH, Lin-Chao S, Li H, Hsieh-Li HM. Stathmin, a microtubule-destabilizing protein, is dysregulated in spinal muscular atrophy. *Hum Mol Genet*. 2010:19(9):1766–1778. https://doi.org/10.1093/hmg/ddq058

Yang Y, Chen B, Dang X, Zhu L, Rao J, Ren H, Lin C, Qin Y, Lin D. Arabidopsis IPGA1 is a microtubule-associated protein essential for cell expansion during petal morphogenesis. *J Exp Bot*. 2019:70(19):5231–5243. https://doi.org/10.1093/jxb/erz284

Zhang C, Liu S, Zhu Q, Zhou Y. A knowledge-based energy function for protein-ligand, protein-protein, and protein-DNA complexes. *J Med Chem*. 2005:48(7):2325–2335. https://doi.org/10.1021/jm049314d

Zhang R, Alushin GM, Brown A, Nogales E. Mechanistic origin of microtubule dynamic instability and its modulation by EB proteins. *Cell*. 2015:162(4):849–859. https://doi.org/10.1016/j.cell.2015.07.012

Zhernov I, Diez S, Braun M, Lansky Z. Intrinsically disordered domain of kinesin-3 Kif14 enables unique functional diversity. *Curr Biol*. 2020:30(17):3342–3351.e5. https://doi.org/10.1016/j.cub.2020.06.039